Journal of Hazardous Materials 261 (2013) 295–306

Contents lists available at ScienceDirect

Journal of Hazardous Materials

journal homepage: www.elsevier.com/locate/jhazmat

Nanoscale zero-valent iron supported on mesoporous silica: Characterization and reactivity for Cr(VI) removal from aqueous solution

Eleni Petala[a,b], Konstantinos Dimos[a], Alexios Douvalis[c], Thomas Bakas[c], Jiri Tucek[b], Radek Zbořil[b], Michael A. Karakassides[a,*]

[a] Department of Materials Science and Engineering, University of Ioannina, GR-45110 Ioannina, Greece
[b] Regional Centre of Advanced Technologies and Materials, Department of Physical Chemistry, Faculty of Science, Palacky University, 17.listopadu 1192/12, 771 46 Olomouc, Czech Republic
[c] Department of Physics, University of Ioannina, GR-45110 Ioannina, Greece

HIGHLIGHTS

- New nanohybrid exhibits magnetic and molecular sieves properties.
- Material shows well dispersed and stabilized ZVI nanoparticles on inorganic support.
- Material demonstrates high Cr(VI) chemical reduction efficiency.

GRAPHICAL ABSTRACT

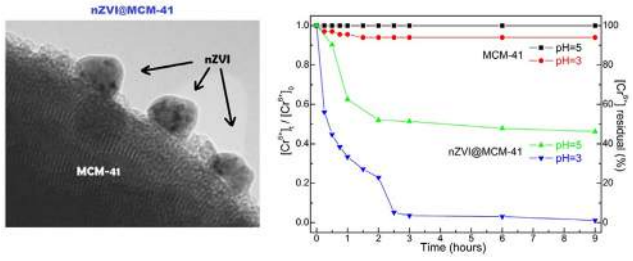

ARTICLE INFO

Article history:
Received 9 March 2013
Received in revised form 18 July 2013
Accepted 21 July 2013
Available online xxx

Keywords:
Nanoscale zero-valent iron
Mesoporous silica
Cr(VI) remediation
Characterization
Kinetics

ABSTRACT

MCM-41-supported nanoscale zero-valent iron (nZVI) was sytnhesized by impregnating the mesoporous silica martix with ferric chloride, followed by chemical reduction with $NaHB_4$. The samples were studied with a combination of characterization techniques such as powder X-ray diffraction (XRD), Fourier-transform infrared (FT-IR) and Mössbauer spectroscopy, N_2 adsorption measurements, transmission electron microscopy (TEM), magnetization measurements, and thermal analysis methods. The experimental data revealed development of nanoscale zero-valent iron particles with an elliptical shape and a maximum size of ~80 nm, which were randomly distributed and immobilized on the mesoporous silica surface. Surface area measurements showed that the porous MCM-41 host matrix maintains its hexagonal mesoporous order structure and exhibits a considerable high surface area (609 m^2/g). Mössbauer and magnetization measurements confirmed the presence of core–shell iron nanoparticles composed of a ferromagnetic metallic core and an oxide/hydroxide shell. The kinetic studies demonstrated a rapid removal of Cr(VI) ions from the aqueous solutions in the presence of these stabilized nZVI particles on MCM-41, and a considerably increased reduction capacity per unit mass of material in comparison to that of unsupported nZVI. The results also indicate a highly pH-dependent reduction efficiency of the material, whereas their kinetics was described by a pseudo-first order kinetic model.

1. Introduction

Since 1991, zero-valent iron (Fe^0 or ZVI) is being used as a reactive material for remediation of contaminated sites due to its great ability to directly or indirectly reduce different types of toxic

* Corresponding author. Tel.: +30 26510 07276; fax: +30 26510 07074.
E-mail address: mkarakas@cc.uoi.gr (M.A. Karakassides).

0304-3894/$ – see front matter © 2013 Elsevier B.V. All rights reserved.
http://dx.doi.org/10.1016/j.jhazmat.2013.07.046

compounds and metal ions such as As(III), Pb(II), Cu(II), Ni(II), Co(II) and Cr(VI) [1–5]. In the environment, iron is always found in its thermodynamically stable oxide forms as under normal conditions, zero-valent iron is unstable and gets oxidized very easily. This fact also explains why metallic iron particles exhibit a high capability in converting various contaminants to less toxic forms [6]. The pathways for contaminant reduction involve: (i) direct reduction at the surface of ZVI, (ii) catalytic reduction through Fe(II) at the surface of corrosion products or (iii) adsorption onto corrosion products [7].

It is well-known that zero-valent iron particle have a core–shell architecture [1,3]. The core consists of metallic iron (α-Fe) while oxides and hydroxides form the shell as a result of oxidation of the iron surface. High activity and efficiency of nZVI particles come from combination of components that form their structure. Core is responsible for the reduction of the contaminants as its oxidation in an aqueous environment generates appropriate reactants such as Fe(II), H/H_2 and iron hydroxides and oxides [8]. However, the presence of the iron oxides causes passivation of the core surface, although in some cases a contaminant should migrate across the film to adsorb on the Fe^0 surface and undergo reduction. Alternatively, the oxide layer should be electronic conductive to allow electron transfer [8]. The sorption and precipitation of the cations depend on some factors, such as the kind of cation, the pH value and concentration [5].

Zero-valent iron can react with oxygen and water following classical electrochemical corrosion reactions in which iron gives electrons to water and Fe(II) gives electrons to O_2 [9]. In addition, ions like Cr(VI) can readily accept the electrons and reduce to lower oxidation states [10,11]. Chromium is a widely used heavy metal in many engineering and chemical industries such as electroplating facilities and tannery industries [12]. It exists mainly in the oxidation states of Cr(VI) and Cr(III) [13]. Hexavalent chromium is considered to be one of the most highly toxic environmental contaminants. Cr(VI) compounds are known to be highly toxic, carcinogenic and mutagenic. They can cause several serious health problems like diseases striking the respiratory tract, male reproductive system, stomach and small intestine. Reduction to Cr(III) followed by precipitation of chromium species may be considered a satisfactory solution in eliminating the toxicity of Cr(VI) because the toxicity of trivalent chromium toward a living cell is 500–1000 times less than hexavalent chromium [14]. However, exposure to excessive doses of Cr(III) for long periods of time may also cause some adverse health effects [15–17]. Therefore, wastewater treatment systems based only on Cr(VI) reduction at acidic pH values, *i.e.*, necessary for high chromium reduction efficiency [18], cannot remove Cr(III) from the solution, since resulting chromium exhibits high solubility at $pH < 4$. Moreover, Fe^0 even though in the form of scrap iron has the advantage not only to reduce Cr(VI)–Cr(III) at $pH \geq 3$ but also to remove the reduced hexavalent chromium from the wastewater as it forms insoluble mixed Cr–Fe (oxy)hydroxide phases *via* its corrosion [18–20]. In addition, the iron corrosion produces iron oxides in which a part of Cr(VI) can also be adsorbed [21].

Zero-valent iron particles, synthesized in the nanoscale form, demonstrate high surface-to-volume ratios, and, thus, high surface activity and increased gravimetric uptake capacity, thought their depletion especially in acidic conditions [7,22]. However, most synthetic ZVI nanoparticles procedures display a significant disadvantage, *i.e.*, the observed aggregation in time, which finally decreases the activity of iron nanoparticles. For this reason, the modification and/or stabilization of ZVI nanoparticles in solid matrices followed by their good dispersion which can lead to steady or even enhanced remediation ability, is deemed necessary. In the past few years, a large number of research works have been emerged focusing on production of more active and stable nZVI particles, simplification of the synthetic procedure and reduction of the cost, stimulating thus their utilization in large-scale applications [23–26].

Among the various heavy metals, Cr(VI) exhibits high sensitivity upon reduction by ZVI [21]. As recently reported [27], the removal efficiency of zero-valent iron ranked from top to bottom: As > Cr > Cu > Hg > Pb > Zn > Cd > Ni, whereas especially Cr(VI) can react with ZVI by more than one mechanism, *i.e.*, reduction, adsorption, co-precipitation. Therefore, Cr(VI) is a suitable candidate for the evaluation of zero valent iron nanoparticles in environmental applications [21].

Aggregation phenomena are reported to be considerably reduced when a matrix or a supporting material is used for the reduction of an iron salt and, additionally, for the production, the homogeneous dispersion, and hosting of nZVI; ZVI nanoparticles synthesized in this way tend to exhibit a narrower size distribution. Therefore, supported nZVI show a higher activity compared to non-supported systems [6,28,29]. The synthesis of nanoscale zero-valent iron has been achieved in the presence of various support materials such as inorganic compounds and clay minerals [30–36], polymers [6,37–39] or other organic compounds [40–42], nanostuctured carbons [43–45], and silica-based molecular sieves [46–49].

Among the support materials, silica-based molecular sieves with uniform pore sizes, such as zeolites, MCM-41 and SBA-15, are particularly interesting as host matrices for loading ZVI nanoparticles, since their nanoporous matrices may additionally affect the catalytic and sorption properties of the hosted nanoparticles. Previous attempts to disperse nanoparticles on silica mesoporous materials were limited to the hexagonal SBA-15 phase. The MCM-41 solid (Mobil Composition of Matter No. 41), a member of the M41S family exhibits regular hexagonal arrays of cylinder-like pores and a variable pore diameter between 1.5 and 20 nm, high crystallinity, and high thermal stability [50,51]. Its large surface area (~1000 m^2/g) makes it ideal for catalytic applications as well as its loading with metal cations [52]. In the present work, we report on the synthesis and stabilization of nZVI in the pores of the MCM-41 matrix. The final materials were tested for their applicability in the remediation of Cr(VI). The main goals of this work were: (a) successful production of stable nZVI with a high gravimetric ratio in the hybrids, (b) high activity of the final materials concerning the reduction of Cr(VI), (c) development of new composite nanomaterials endowed with improved properties through synergetic effects, and (d) materials which can be easily separated and collected by an external magnetic field.

2. Materials and methods

2.1. Materials

The following reagents were used as purchased without further purification: tetraethylorthosilicate (TEOS) 98% from Sigma–Aldrich (131903), aqueous ammonia solution (NH_3) 25 wt% from Fluka (09860), cetyltrimethylammonium bromide (CTAB) 95% from Sigma–Aldrich (855820), ethanol (EtOH) 99.5% from Panreac (121086.1212), hydrochloric acid (HCl) 1 N from Riedel de Haën (35328), analytical grade acetone 99.95% from Fisher Scientific (A/0600/17), phosphoric acid (H_3PO_4) 85% from Sigma–Aldrich (215104), potassium dichromate ($K_2Cr_2O_7$) from Sigma–Aldrich (P2588), 1,5-diphenylcarbazide from Aldrich (42860), sodium borohydride ($NaBH_4$) from Merck (8.06373) and iron (III) chloride hexahydrate ($FeCl_3 \cdot 6H_2O$) from Sigma–Aldrich (207926).

2.2. Synthesis of MCM-41

The MCM-41 sample was synthesized by hydrolyzing 50 g of TEOS, added to one liter polyethylene bottle containing 417.5 g of H_2O, 268.5 g of NH_3 (25 wt%) and 10.5 g of CTAB. The resulting mixture was stirred for 30 min. The product was retrieved after heat treatment at 80 °C for 96 h. It was filtered, rinsed with cold EtOH and finally placed on a plate for air-drying (sample: MCM-41). The template was removed by calcination at 550 °C for 5 h with a 2 °C/min heating rate.

2.3. Synthesis of nZVI

One gram of $FeCl_3{\cdot}6H_2O$ was dissolved in 50 mL of EtOH. The reducing agent was prepared by dissolving 1 g of $NaBH_4$ in 50 mL of deionized water. The borohydride solution was added drop-wise to the ferric solution while swirling by hand. Black agglomerated particles appeared immediately indicating the presence of zero-valent iron. After complete addition of the borohydride solution, the mixture was left to settle for 15 min. The mixture was centrifugated and the separated particles were washed with EtOH three times and dried in vacuum (sample: nZVI). Experimental parameters such as reaction time, reactant concentrations and volumes were kept constant in order to produce samples with consistent properties.

2.4. Preparation of nZVI supported on MCM-41

The formation of the nZVI onto the inner surface of MCM-41 was carried out by wet impregnation technique. 1.5 g of ferric chloride ($FeCl_3{\cdot}6H_2O$) was dissolved in 10 mL of absolute ethanol and was dropped on 0.7 g of the mesoporous material. The mixture was heated at ~80 °C up to the evaporation of the solvent and the obtained powder was dispersed in 100 mL of absolute ethanol. The reducing agent was prepared by dissolving 1.5 g of $NaBH_4$ in 150 mL of deionized water and was added drop-wise to the MCM-41-Fe^{3+} solution while swirling by hand. After the complete addition of the borohydride solution, the mixture was left to settle for 15 min. The mixture was centrifugated and the separated particles were washed with absolute ethanol three times and dried in vacuum (sample: nZVI@MCM-41). In this case, a lower concentration of the reactive agent was used in order to avoid destruction of the MCM-41 structure. Dissolution of MCM-41 framework can be caused by a slow reaction between sodium borohydride and ethanol.

2.5. Characterization

The θ–2θ X-ray powder diffraction data (XRD) were collected with a D8 Advance Bruker diffractometer using Cu Kα (40 kV, 40 mA, λ = 1.54178 Å) radiation. Diffraction patterns were collected in the 2θ range from 1.5° to 80°, in steps of 0.02° and 2ʏs counting time per step. Pellets of pulverized samples dispersed in KBr were used for recording Fourier transform Infrared spectra on a Perkin Elmer GX Fourier transform spectrometer in the frequency range of 400–4000 cm^{-1}. The reported spectra are an average of 64 scans at 2 cm^{-1} resolution. Thermo-gravimetric analysis (TG) and differential thermal analysis (DTA) were performed using a Perkin Elmer Pyris Diamond TG/DTA instrument. Samples of ~4 mg were heated in not-flowing atmospheric air from 25 to 750 °C with a 5 °C/min heating rate.

The nitrogen adsorption–desorption isotherms were measured at 77 K on a Sorptomatic 1990, thermo Finnigan porosimeter. Specific surface areas (S_{BET}) were determined with the Brunauer–Emmett–Teller (BET) method using adsorption data points in the relative pressure P/P_0 range from 0.01 to 0.30. Surface areas (S_t) were also determined from *t*-plots which were constructed using nitrogen adsorption data with the de Boer standard. Mesoporous surface area (S_{meso}) and volume (V_{meso}) were also determined from V_a–*t*-plots. Total pore volume (V_{pore}) was estimated from the adsorbed amount at a relative pressure of 0.99. The desorption branches of the isotherms were used for the pore size calculations according to the Kelvin equation, *i.e.*, $r_k \sim 4.146/(\log(P_0/P))$ (Å), where P_0 is the saturated vapour pressure in equilibrium with the adsorbate condensed in a capillary or a pore, P is the vapour pressure of a liquid contained in a cylindrical capillary, and r_k is the Kelvin radius of the capillary or pore. The Kelvin equation was used according to the BJH method for calculation of core radii and the pore size distribution (PSD) of the samples. All samples used for the surface analyses were outgassed at 150 °C for 16 h under high vacuum (10^{-5} mbar) before the measurements.

Transmission electron microscopy (TEM) observations were performed on a JEOL JEM-2010 transmission electron microscope equipped by a LaB_6 cathode (accelerating voltage of 200 kV; point-to-point resolution of 0.194 nm). A drop of high-purity distilled water, containing the ultrasonically dispersed particles, was placed onto a Holey Carbon film supported by a copper-mesh TEM grid and air-dried at room temperature.

^{57}Fe Mössbauer spectra were collected in transmission geometry at 77 K, using a constant-acceleration spectrometer, equipped with a ^{57}Co(Rh) source kept at room temperature (RT) and a liquid N_2 bath Mössbauer cryostat (Oxford Instruments). Velocity calibration of the spectrometer was carried out using metallic α-Fe at RT and all isomer shift (δ) values are given relative to this standard. Magnetization (M) measurements were performed on a superconducting quantum interference device (SQUID) magnetometer (Quantum Design, MPMS XL-7). The hysteresis loops were collected at temperatures of 5 and 300 K in external applied magnetic fields (B) ranging from −7 to +7 T. The zero-field-cooled (ZFC) and field-cooled (FC) magnetization curves were recorded on warming the samples in the temperature range from 5 to 300 K under external magnetic fields of 0.01 and 0.1 T after cooling in zero magnetic field and on cooling under the same fields, respectively.

2.6. Batch experiments for the reduction of Cr(VI)

In order to test the reduction capacity of nZVI and MCM-41-supported nZVI, appropriate amount of each sample with the same iron content (18 mg of nZVI@MCM-41 and 3.5 mg nZVI) was added to 100 mL solution of $K_2Cr_2O_7$ in distilled water (concentration of Cr(VI): 6 mg/L) previously stirred at room temperature for 12 h in a closed vessel. Tests were performed at two different pH values (pH = 3 and pH = 5) and various reaction times. The pH of the suspensions was adjusted to 5 or 3 by adding hydrochloric acid solution (1 N). During the reaction, at different periods, a volume of the under study suspension (5 mL) was withdrawn and centrifuged. From the resulting supernatant Cr(VI) solution a volume of 0.3 mL was used for colorimetric measurements, while the solid and the rest unused centrifuged solution were returned to the suspension. The Cr(VI) concentration of the solution was then determined by using the 1,5-diphenylcarbazide method [53]. The 1,5-diphenylcarbazide method is based on the reaction of Cr(VI) cations with 1,5-diphenylcarbazide molecules leading to the formation of a red-purple chromium 1,5-diphenylcarbazide complex. Diphenylcarbazide solution was prepared by dissolving 0.025 g of 1.5-diphenylcarbazide in 10 mL of analytical grade acetone. The solution was stored in a closed flask at 4 °C up to 7 days. Phosphoric acid solution was prepared by diluting 0.5 mL of concentrated phosphoric acid in 10 mL of deionized water. To each tested solution (0.3 mL), 160 μL of the diphenylcarbazide solution and 80 μL of the phosphoric acid solution were added (total volume adjusted at 3 mL with 2.460 mL H_2O). The solution was swirled and left

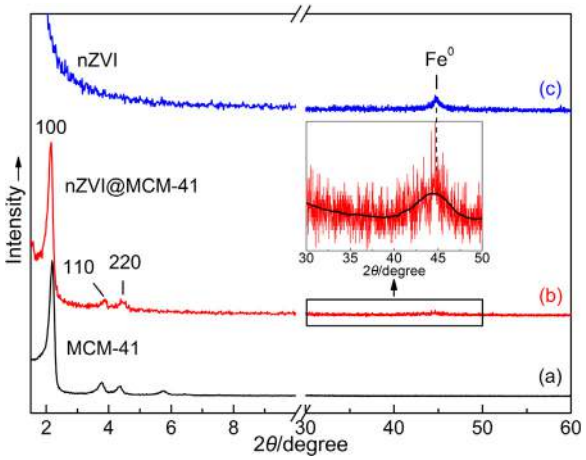

Fig. 1. X-ray diffraction patterns of MCM-41 (a), supported zero-valent iron nanoparticles on mesoporous silica, nZVI@MCM-41 (b), and unsupported nZVI (c). Inset shows the marked part of XRD pattern of nZVI@MCM-41 in magnification.

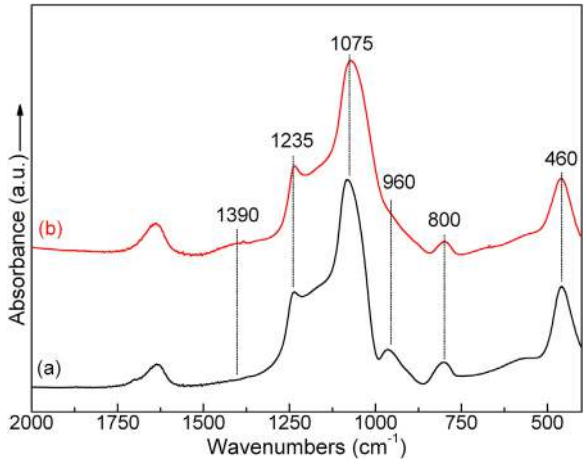

Fig. 2. FT-infrared spectra of MCM-41 (a) and nZVI@MCM-41 (b) sample.

for 10 min to allow color development and then the solution's concentration was determined spectrophotometrically by using UV–vis spectroscopy at 540 nm using a calibration curve. Absorption spectra of solutions were measured using a 10 mm optical path quartz vesicle. UV–vis spectra were recorded on a Shimadzu UV-2401PC two beam spectrophotometer in the range of 350–700 nm, at a step of 0.5 nm, using combination of deuterium and halogen lamps as sources. The calibration curve was initially determined by using the absorbance spectra of standard chromium solutions (Supporting Information Figs. S1 and S2). The total chromium concentration was determined by oxidizing any trivalent chromium with potassium permanganate [18,54], followed by analysis as hexavalent chromium. Trivalent chromium was determined from the difference between total and hexavalent chromium. In addition, because pH has a strong effect on Cr(VI) sorption and reduction, the pH value of the suspension was also measured at different periods.

2.7. Adsorption isotherms

Adsorption isotherms of Cr(VI) on MCM-41 were determined using batch equilibrium of 0.145 g of dosage materials in 100 mL Cr(VI) solution at various initial concentrations. All experiments were varied out in a stealing-steel cooling bath whereas the reaction mixture was kept under suspension using a magnetic stirrer located under the bath base. During the experiments the solution temperature was kept constant at 25 °C by means of cooling water. After equilibrium, the solution was centrifuged and filtered with filter paper while the supernatant was measured by the diphenylcarbazide method. The adsorbed amount was calculated from the difference between initial (C_0) and equilibrium (C_e) concentration according to the equation $q_e = [(C_0 - C_e) \times V]/m$, where V is the total volume of the solution (mL) and m is the mass of adsorbent (g) [55].

The variation of pH during the reaction of Cr(VI) was also measured *versus* time. Appropriate amount of each sample (14.5 mg for MCM-41, 18 mg for nZVI@MCM-41, and 3.5 mg for nZVI) was added to 100 mL Cr(VI) 6 mg/L solution and pH was measured until it reached a plateau.

3. Results and discussion

3.1. Structural and textural characterization

Fig. 1 shows the X-ray diffraction pattern from a powder of nZVI and that of the same nanoparticles supported on mesoporous silica. As it is evident, the XRD pattern of the nZVI@MCM-41 sample displays three reflection peaks, typical of the MCM-41 mesoporous materials. They arise from the quasi-regular arrangement of the mesopores in the bulk material. Specifically, they show a characteristic strong reflection at low scattering 2θ angles, corresponding to a d_{100} spacing at about 40 Å. Furthermore, the pattern of nZVI@MCM-41 sample clearly displays the higher order 110 and 200 reflections suggesting that the hexagonal structure of the support matrix remains unimpaired upon the nanoparticle growth on its surfaces [56]. Besides, the characteristic peak at $2\theta = 44.9°$ in the XRD patterns of nZVI and nZVI@MCM-41 sample indicates the presence of ion predominantly in the Fe^0 state, as reflections due to iron oxides such as magnetite, γ-Fe_2O_3 or hematite ($2\theta \sim 36°$) were not observed in both patterns.

The infrared spectra of MCM-41 and nZVI@MCM-41 samples are shown in Fig. 2. Both spectra (a and b) display bands at 1235, 1075, 800 and 460 cm^{-1}. Bands at similar frequencies in the spectra of crystalline and amorphous SiO_2 have been assigned to characteristic vibrations of Si—O—Si bridges cross-linking the silicate network [57–60]. Thus, the stronger bands at 1235 at 1075 cm^{-1} can be assigned to the asymmetric stretching mode vibrations of the Si—O—Si group whereas the appearance of the two maxima can be related to the LO and TO components of its vibration [61]. The bending motion of oxygen in the same bridge is responsible for the band at 800 cm^{-1} (motion along the bisector of the Si—O—Si bridging group) while the rocking motion of bridging oxygens perpendicular to the Si—O—Si plane can be correlated with the 460 cm^{-1} band. On the other hand, only the spectrum of MCM-41 sample exhibits the band at 960 cm^{-1} which can be assigned to vibrations of Si—O^- and Si—OH bonds in the silicate tetrahedral units. In the spectrum of nZVI@MCM-41, a significant reduction of absorption in this spectral area can be attributed to the formation of Si—O^-—Fe bonds. Moreover, the effect of $NaBH_4$ on infrared vibrations of silanols groups was found to be negligible under the used conditions whereas the broad absorption band at 1390 cm^{-1} observed in the spectrum of nZVI@MCM-41 can be correlated with the presence of borate species produced during the iron nanoparticle synthesis.

Fig. 3 shows the DTA and TG curves recorded under air for the MCM-41 matrix before (a) and after the nZVI upgrowth (b). The pristine MCM-41 matrix exhibits a smooth DTA curve without any remarkable exothermic or endothermic peak and a weight loss less than 0.5% as the mesoporous silica was treated at 550 °C for 5 h at its last step of synthesis. On the other hand, the TGA curve of nZVI@MCM-41 shows a weight loss of ~7 wt% at low temperatures (up to 150 °C) followed by a weight increase of ~4 wt% in the

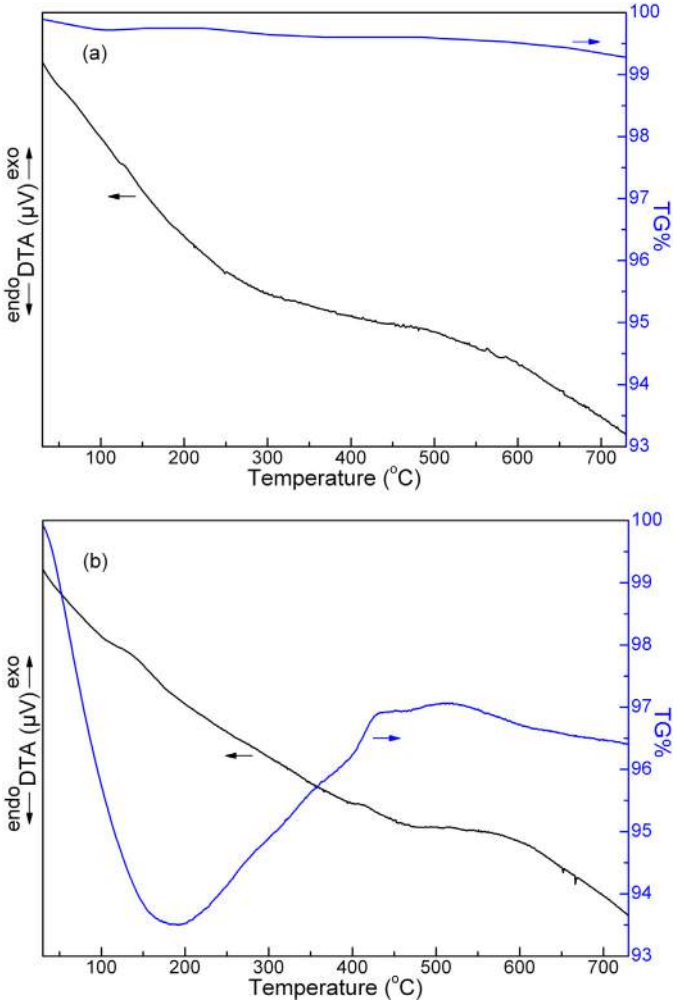

Fig. 3. DTA/TG diagrams of MCM-41 (a) and nZVI@MCM-41 (b) sample.

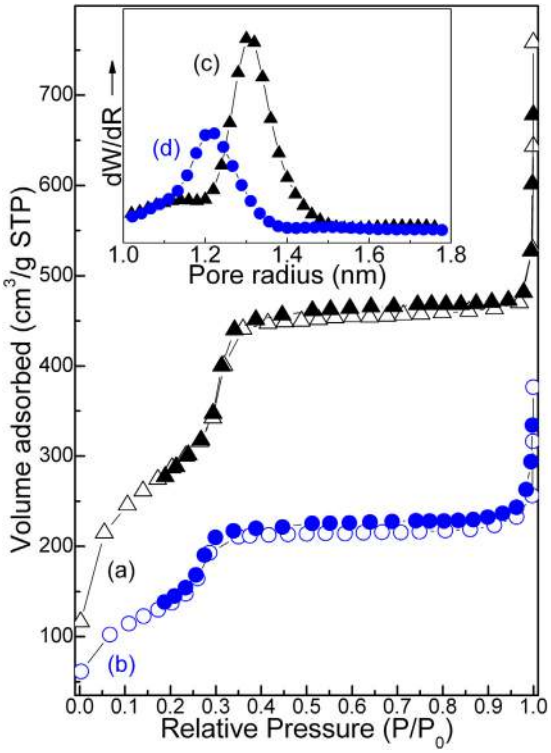

Fig. 4. Nitrogen adsorption–desorption isotherms for MCM-41 (a) and nZVI@MCM-41 (b) sample. Inset: pore size distributions calculated from nitrogen desorption branch for MCM-41 (c) and nZVI@MCM-41 (d) sample.

temperature range of 200 to 500 °C. The ~7 wt% loss at low temperatures is assigned to ethanol and water desorption [62], while the ~4 wt% increase of the sample could be attributed to nZVI oxidation which were anchored on the silicate matrix. The observed mass increase is also related to a weak exothermic peak observed at 400 °C in the DTA curve of nZVI@MCM-41 sample, implying the nZVI oxidation. This assignment is in accordance with the recent study on thermal oxidation of iron nanoparticles [6,63]. Furthermore, taking into account the ~4% weight increase in the TGA signal and the fact that at temperatures >200 °C the thermal oxidation of Fe^0 in air gives Fe_2O_3, the total zero-valent iron-content of nZVI@MCM-41 was determined at about ~9.3% of its total mass.

The surface area and the pore structure of MCM-41 and nZVI@MCM-41 samples were determined from the nitrogen isotherms analysis. As it is shown in Fig. 4, both samples exhibit type-IV isotherms, characteristic of mesoporous materials. The presence of a sharp sorption step in these adsorption curves, near to a 0.3 value of P/P_0, indicates that the two solids possess a well defined array of regular mesopores. Based on these data, the specific surface area (S_{BET}) for the MCM-41 pristine sample was calculated to be 1060 m^2/g, the mean pore diameter 2.6 nm, and the total pore volume 0.79 cm^3/g (Table 1). On the other hand, the nZVI@MCM-41 sample, which was prepared using the above MCM-41 as a matrix, displayed similar type-IV adsorption/desorption isotherms but showed a lower surface area of ~609 m^2/g, mean pore diameter of ~2.4 nm and a total pore volume of 0.32 cm^3/g, which provides evidence that its pores are filled with zero-valent iron nanoparticles. Alternatively, these data suggest that the pore access of nZVI@MCM-41 is limited because of the formation of Fe^0 nanoparticles with sizes larger than 3 nm on the external surfaces of the matrix.

Fig. 5 shows the TEM images of iron nanoparticles supported on the MCM-41 matrix (a and b) and that of as-prepared Fe^0 nanoparticles (c) after reduction of $FeCl_3$ in aqueous solution by $NaBH_4$ for comparison purposes. It is evident that nanoparticles, elliptical in shape and with a maximum size of ~80 nm, were randomly distributed and immobilized on the mesoporous silica surface. These nanoparticles seem to possess a core–shell structure (Fig. 5b) according to the core–shell model of nZVI [1] in which the core is made up mainly of Fe^0 and the shell is largely of iron oxides/hydroxides origin, formed from the oxidation of zero-valent iron. TEM analysis of image (b) supports this view (number 1 and 2 indicate the regions of nanoparticles which are attributed to Fe^0 core and oxide shell, respectively). In addition, the linear array of mesoporous silica channels is clearly observed in the region of number 3 of Fig. 5b, indicating, in agreement with the XRD results, that the sample keeps the hexagonal mesoporous order structure of MCM-41 support. It should be noted that the degree of aggregation of these particles is limited in contrary to that exhibited by ZVI nanoparticles synthesized without any support (see Fig. 5c for comparison).

From TEM images it can also be calculated the Fe^0 content in the nZVI particles equal to 47.82 wt% (calculations in Supporting Information for Fig. S3), which is a value in good agreement with literature [55,64]. The above percentage, combined with the TGA data, also suggests that the total nZVI wt% content of the hybrid material (nZVI@MCM-41) is 19.45% (as the iron of the shell is already oxidized and would not attribute to the observed weight increase in the TGA signal) which means that the same iron content for the batch experiments is 180 mg/L for the hybrid material and 35 mg/L for the nZVI.

Table 1
Textural properties of MCM-41 and nZVI@MCM-41 sample.

Sample	S_{BET} (m^2/g)[a]	S_t (m^2/g)[b]	S_{meso} (m^2/g)[b]	V_{pore} (cm^3/g)[c]	V_{meso} (cm^3/g)[b]	d_{BJH} (nm)[d]
MCM-41	1060	1052	1040	0.79	0.72	2.6
nZVI@MCM-41	609	612	592	0.39	0.32	2.4

[a] Total specific surface area (S_{BET}) form multi-point BET analysis.
[b] Total surface area (S_t), mesoporous surface area (S_{meso}) and mesoporous volume (V_{meso}) determined form t-plots (standard: de Boer).
[c] Total pore volume (V_{pore}) estimated from the adsorbed amount at relative pressure of 0.99.
[d] Mean pore diameters (d_{BJH}) determined form BJH analysis of the desorption data.

3.2. Magnetic properties and Mössbauer study of pristine and treated samples with Cr^{6+} solutions

^{57}Fe Mössbauer spectra of nZVI@MCM-41 sample as well as samples after treatment with aquatic Cr^{6+} solution and after treatment in water (for 24 h), recorded at 77 K, are shown in Fig. 6. The spectrum of the initial sample shows magnetically split and quadrupole split contributions. A model of five independent spectral components was used to fit this spectrum and the resulting Mössbauer hyperfine parameters are listed in Table 2. In particular, the resonant lines of the central magnetically split contributions seem to show a superposition of a major part with broad resonant lines (component 1) and a minor part with narrow resonant lines (component 3). The δ and hyperfine magnetic field (B_{hf}) values of these two components correspond to iron atoms having metallic characteristics. These components represent the iron atoms situated at the metallic cores of the ZVI nanoparticles. The differences between the corresponding δ and B_{hf} values and the line-width of these two components reflect the difference in the sizes of the ZVI nanoparticles. The smaller nanoparticles, which are represented by component 1, show superparamagnetic relaxation effects, as they are drastically influenced by thermal agitation due to their reduced sizes [65]. On the other hand, the larger nanoparticles, represented here by component 3, possess hyperfine parameters resembling those of bulk metallic iron [66] due to their increased sizes.

The main quadrupole split central part of the spectrum is fitted by component 2. The hyperfine parameters of this component correspond to a Fe^{3+} in a high-spin ($S = 5/2$) state and represent ferric ions in oxide or hydroxide phases [67]. These phases constitute most probably the shell of the nanoparticles, which is formed during their preparation or by oxidation when the nanoparticles get in contact with atmospheric oxygen and moisture. The paramagnetic (only quadrupole split) state of this components suggests that the shell of the nanoparticles is composed mainly of iron oxide/hydroxide such as ferrihydrite which may have magnetic ordering temperatures lower than 77 K [67] or these shell phases show superparamagnetic phenomena due to their reduced dimensions (thin shells).

A minor broad magnetically split contribution is also evident by its two outer higher-velocity resonant lines near ±8 mm/s (component 4), which emerge from the background. Its δ value corresponds to Fe^{3+} in a high-spin ($S = 5/2$) state, and its high B_{hf} value (see Table 2) suggests that it represents such ions in iron oxide/hydroxide phase constituting most probably the shell of the larger ZVI nanoparticles, whose core is represented in the spectrum by component 2. Finally, a minor quadrupole split contribution (component 5) with Fe^{2+} high-spin ($S = 2$) state characteristics (see Table 2) was introduced to the fitting model in order to cover the missing absorption intensities near −0.5 and +2.5 mm/s. This component corresponds to partially oxidized iron ions, most probably in some minor impurity iron oxide phases produced during the preparation procedure.

The spectrum of the nZVI@MCM-41 after treatment with aquatic Cr^{6+} solution sample (Cr^{6+}-reacted sample) resembles that of the corresponding initial sample and is fitted using the same model. However, the comparison between the resulting absorption areas of the components used to fit the two spectra reveals important differences that reflect the effect of the redox reaction between the Cr^{6+} ions in the solution and the nZVI. In particular, component 1 in the Mössbauer spectrum of the Cr^{6+}-reacted sample which represents the core of the nZVI, looses absorption area, while component 3, which represents their shell, gains absorption area, relative to the areas found for the corresponding components of the spectrum of the as-made sample (see Table 2). All the other components in the spectrum of the Cr^{6+}-reacted sample retain essentially the same relative absorption areas they had in the as-made sample. This result

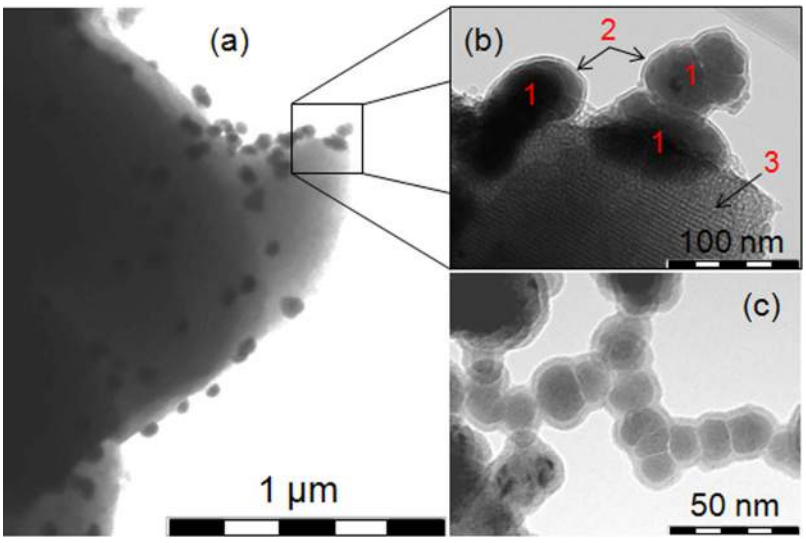

Fig. 5. TEM images of nZVI@MCM-41 (a and b) and nZVI (c) sample.

Table 2
Values of the hyperfine parameters derived from the best fits of the hybrid nZVI@MCM-41 as-made, Cr^{6+}-reacted and water-treated samples, recorded at 77 K, where δ is the isomer shift (relative to α-Fe at RT), $\Gamma/2$ is the half width at half maximum, ΔE_Q is the quadrupole splitting, 2ε is the quadrupole shift, B_{hf} is the hyperfine magnetic field, ΔB_{hf} is the spreading of B_{hf} and A is the relative spectral absorption area for each component. The components discussed in the text and their assignments are also listed. Typical errors are ±0.02 mm/s for δ, $\Gamma/2$, ΔE_Q and 2ε and ±5% for A.

Sample	Component	δ (mm/s)	$\Gamma/2$ (mm/s)	ΔE_Q or 2ε (mm/s)	B_{hf} (T)	ΔB_{hf} (T)	A (%)	Assignment
As-made	1	0.23	0.29	−0.04	27.9	6.3	62	Fe^0 in core (small ZVI)
	2	0.47	0.30	0.81	–	–	23	Fe^{3+} in shell (small ZVI)
	3	0.12	0.17	−0.02	33.8	0.4	6	Fe^0 in core (large ZVI)
	4	0.47	0.18	0.00	50.8	4.3	6	Fe^{3+} in shell (large ZVI)
	5	1.12	0.35	2.91	–	–	3	Fe^{2+} in impurities
Cr^{6+}-reacted	1	0.26	0.29	−0.05	28.1	6.5	51	Fe^0 in core (small ZVI)
	2	0.47	0.30	0.80	–	–	34	Fe^{3+} in shell (small ZVI)
	3	0.11	0.18	−0.03	33.6	0.6	5	Fe^0 in core (large ZVI)
	4	0.47	0.18	0.00	49.0	4.3	6	Fe^{3+} in shell (large ZVI)
	5	1.12	0.35	2.79	–	–	4	Fe^{2+} in impurities
Water-reacted	A	0.47	0.29	0.79	–	–	85	Fe^{3+} as in shell
	B	0.47	0.16	−0.01	31.6	8.9	15	Fe^{3+} as in shell

is a direct proof that during the redox reaction, Cr^{6+} ions diffusing through the ZVI nanoparticles shell are reduced to Cr^{3+} by oxidizing the metallic core Fe^0 atoms to Fe^{3+} ions, increasing thus the shell thickness. On the other hand, the large ZVI nanoparticles (represented by components 3 and 4) stay almost inert in this reaction.

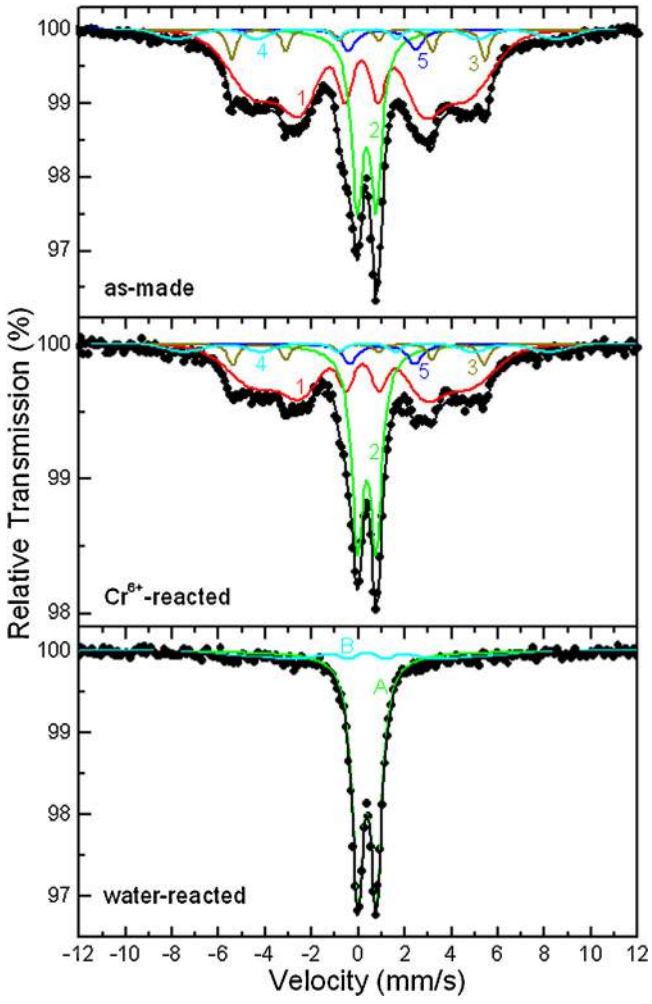

Fig. 6. ^{57}Fe Mössbauer spectra of the hybrid nZVI@MCM-41 as-made, Cr^{6+}-reacted and water-treated samples recorded at 77 K. The points correspond to the experimental data and the continuous lines to the components used to fit the spectra. The numbers and letters correspond to the components discussed in the text and Table 2.

Thus, the second important conclusion is that the size of nZVI is a significant factor for the yield of the reduction of Cr^{6+} in the solution – the smaller ZVI particles are simultaneously the most active to this procedure as well.

Comparison of the former two spectra with the spectrum recorded after treating the as-made sample with water reveals additional information on the dynamics of the redox reaction. This spectrum is composed of two components, one major paramagnetic doublet (component A) and one minor very broad magnetic sextet (component B), whose values of the hyperfine parameters are characteristic of Fe^{3+} ions only and resemble much those of components 2 and 4 used to fit the spectra discussed above (see Table 2). This result indicates that degradation of the metallic Fe^0 phase during the hydrolysis reaction causes all iron atoms to be fully oxidized to Fe^{3+}, transforming completely the core of the ZVI nanoparticles to the oxide/hydroxide phases of the shell through oxygen and water molecule diffusion. However, it is important to note that the appearance of characteristic Fe^0 components in the spectrum of the Cr^{6+}-reacted sample denotes a preservation of the Fe^0 cores. This suggests that in the case of the reaction of ZVI nanoparticles with Cr^{6+} ions in the corresponding aquatic solution, diffusion of Cr ions in the shell of the nanoparticles forms a shell with an iron-chromium oxide/hydroxide composition, most probably situated near the core that prevents the remaining Fe^0 core from further oxidation. On the other hand, it can be accompanied with a saturation effect, suppressing the ability of these modified ZVI nanoparticles to reduce additional Cr^{6+} ions existing in the solution.

The physical properties of nZVI@MCM-41 sample can be revealed from its magnetization measurements. Fig. 7 shows the hysteresis loops of this sample recorded at 300 and 5 K. Ferromagnetic response with maximum magnetizations (at 7 T) of ~36.8 and ~43.7 Am^2/kg at 300 and 5 K, respectively, are observed, while saturation is not achieved at both temperatures, as a non-vanishing dM/dB slope is evident at the high applied magnetic field region. In addition, this slope seems to be higher for the measurement at 5 K compared with that observed at 300 K. Moreover, hysteresis behavior is clearly seen in the insets of Fig. 7, with the values of the coercive fields of ~54.7 and ~73.5 mT at 300 and 5 K, respectively. The saturation magnetization of pure bulk metallic iron varies from ~218.0 to ~221.9 Am^2/kg between 300 and 5 K, respectively, while its coercivity lies in the range of 1.0–2.0 mT [68]. Consequently, the loop characteristics of the nZVI@MCM-41 sample, observed both at 300 and 5 K, reflect the size effect of the ZVI particles, as the non-vanishing high field dM/dB slope, the decrease in the saturation magnetization and the increase in the coercive field are identifying features of their nanostructured nature. However, the large decrease in the saturation magnetization could be attributed also

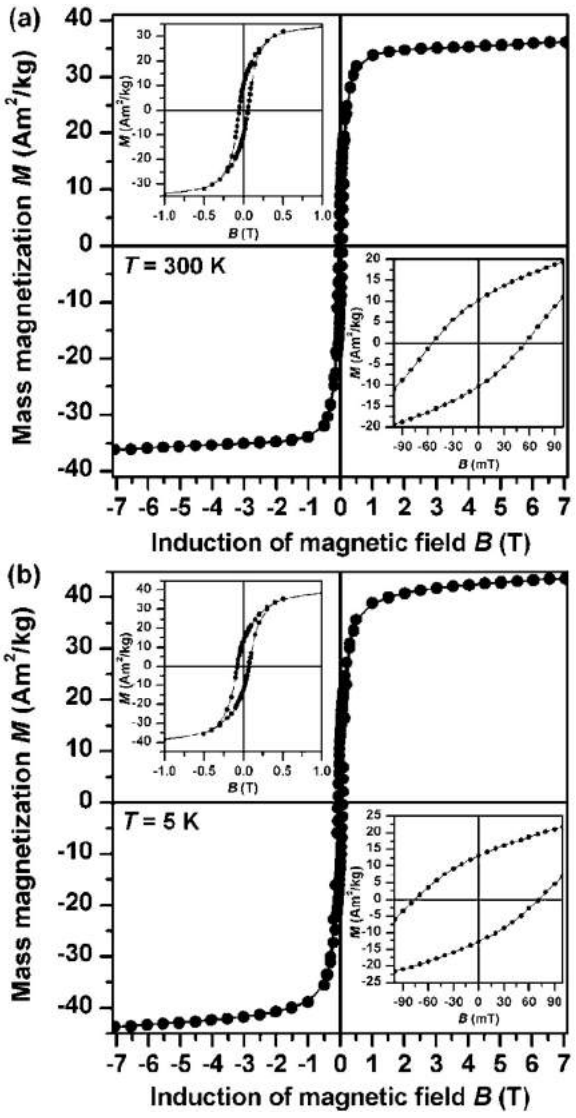

Fig. 7. Hysteresis loops of nZVI@MCM-41 sample recorded at 300 K (a) and 5 K (b).

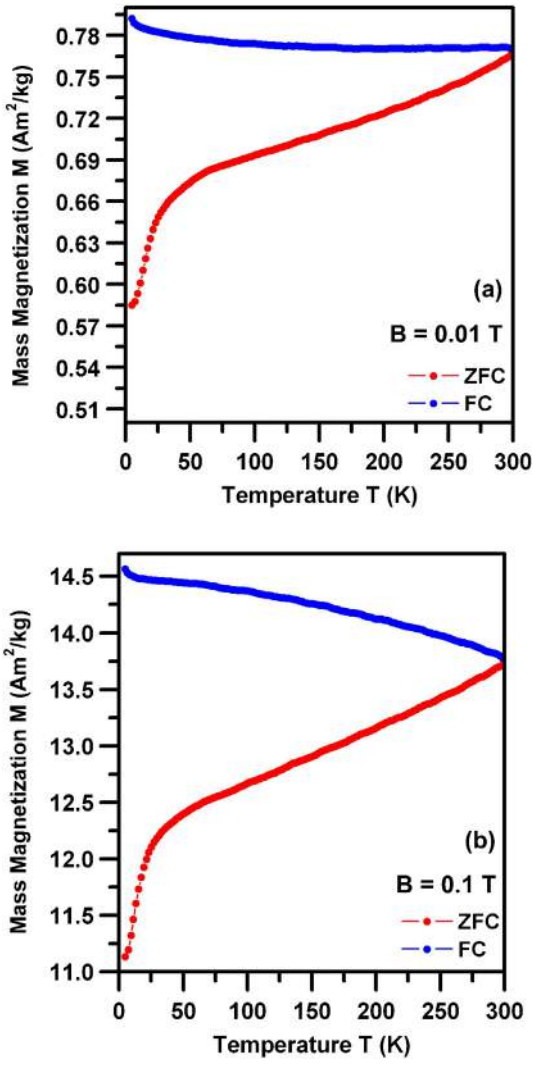

Fig. 8. ZFC and FC magnetization curves of the nZVI@MCM-41 sample recorded at 0.01 (a) and 0.1 T (b).

to the presence of the additional masses of the MCM matrix, as well as of the oxide/hydroxide shell phases in the sample, which provide diamagnetic and antiferromagnetic contributions, respectively.

The ZFC/FC magnetization curves of the nZVI@MCM-41 sample, depicted in Fig. 8, confirm the conclusions derived from the hysteresis loops measurements. In the ZFC magnetization branch, recorded under applied magnetic fields of 0.01 and 0.1 T, the magnetization values show a steep increase with increasing temperature, followed by a more gradual increase above about 50 K. On the contrary, FC magnetization curves display a relative stable increase in the magnetization values with decreasing temperature which is followed by a steep increase at temperatures below 10 K. This is a typical behavior found for such core–shell nanoparticles composed of a ferromagnetic metallic core and an oxide/hydroxide shell [67]. In addition, this indicates that the ZVI nanoparticles in the studied system appear in a range of sizes that restrain them from adopting complete superparamagnetic characteristics.

3.3. Cr(VI) reduction

The capacity of the nZVI@MCM-41 sample on hexavalent chromium removal was estimated by conducting a series of batch experiments. Fig. 9a displays the removal kinetics at 6 mg/L of initial concentration in Cr(VI) of the aqueous solution as a function of reaction time for 180 mg/L dosage and two different pH values (3 and 5). The reaction capacity of the pristine MCM-41 is also shown in the same figure for comparison purpose. The kinetics of the removal process was simulated using the pseudo first-order model [69] expressed by the equation:

$$dC/dt = -k_{obs} \cdot C \quad (1)$$

where C is the concentration of contaminant (*i.e.*, Cr(VI)) in the aqueous phase (mg/L) and k_{obs} is the observed rate constant of the pseudo first-order reaction (h^{-1}). According to this model, k_{obs} is the product of $K_{SA} \cdot \rho_m \cdot a_s$ where K_{SA} is the surface-area normalized rate coefficient (L/h m^2), ρ_m is the mass concentration (g/L) and a_s is the specific surface area (m^2/g) of the used material respectively. Since K_{SA}, ρ_m, and a_s are constant for a specific reaction, their product can be expressed with only one parameter, *i.e.*, k_{obs}. Integration of Eq. (1) gives:

$$\ln\left(\frac{C}{C_0}\right) = -k_{obs} \cdot t \quad (2)$$

where $C_0 = [Cr(VI)]_0$ and $C = [Cr(VI)]_t$ are Cr(VI) concentrations in the solution after 0 and t hours of reaction and k_{obs} is the observed rate constant of the pseudo first-order reaction (h^{-1}). The plots of $\ln([Cr(VI)]_t/[Cr(VI)]_0)$ *versus* time produced linear lines (see Fig. 9b)

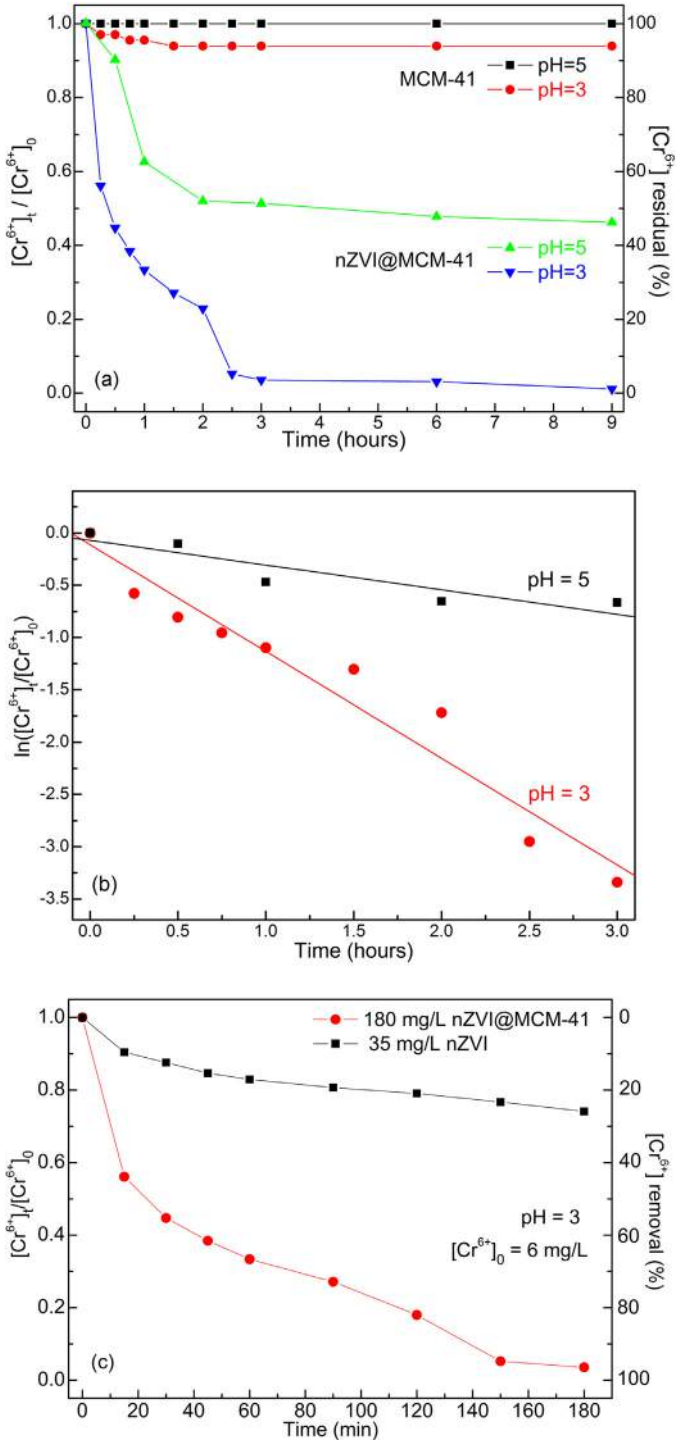

Fig. 9. (a) Effect of initial pH value (5 and 3) on the Cr(VI) removal efficiency by pristine MCM-41 and nZVI@MCM-41 sample and (b) pseudo-first-order kinetics for reduction of Cr(VI) by nZVI@MCM-41 (nZVI@MCM-41 dose was 180 mg/L and initial Cr(VI) concentration was 6 ppm). (c) Cr(VI) removal efficiency of nZVI@MCM-41 sample (dosage of 18 mg containing ~3.5 mg of nZVI) in comparison to that of unsupported nZVI (same dosage of 3.5 mg nZVI).

with correlation coefficients (R^2) reaching a value more than 0.97, indicating that the rate of chromium removal fitted well this model. The k_{obs} values are equal to the slope of the line by plotting $\ln([Cr(VI)]_t/[Cr(VI)]_0)$ *versus* time; k_{obs} were found to be 1.02 and 0.332 h^{-1} for pH = 3 and 5, respectively. The Gibbs free energy (ΔG^0) was also calculated for nZVI@MCM-41 hybrid at room temperature at pH = 3 and 5 using the equations $K_D = q_e/C_e$ and $\Delta G^\circ = -R{\cdot}T{\cdot}\ln K_D$ where C_e is the equilibrium concentration (mg/mL), q_e is the amount of Cr(VI) removed at equilibrium (mg/g), K_D is the distribution coefficient (mL/g), R is the gas constant (8.134 J/mol K) and T is the temperature (K) [70]. Employing this equation, we arrived at −28.91 kJ/mol (pH = 3) and −20.77 kJ/mol (pH = 5). From these negative values, one can conclude that the removal process is spontaneous and thermodynamically favorable.

It is well known that the removal capacity and mechanism of zero-valent iron nanoparticles is strongly affected by the pH. At pH = 3, Cr(VI) was completely eliminated within 3 h; however, at higher pH values, passivation of the surface of iron particles probably occurred, limiting the further removal capability. While the zero-valent iron particles undergo oxidation, iron oxide/hydroxide species are formed on the surface of the hybrid material. The solubility of these oxides/hydroxides is not favorable at high values of pH while their formation is related also with the initial concentration of the Cr(VI). Generally, it has been reported that the capacity and the reaction rate of ZVI depend on the total surface area, the type of contaminant, the initial concentration of iron and the pollutant, the presence of other oxidants such as oxygen and nitrate, and on solution chemistry such as solution pH [71].

Besides, Cr(VI) can be reduced by Fe(II) or atomic/molecular hydrogen (H/H_2), which is derived from the oxidation of zero valent iron, and by electrons originating directly from the Fe^0 core, if its oxide layer shell is conductive [72], since the outer oxide film on the ZVI particles restricts the accessibility between iron core and Cr(VI) species. On the other hand, as the Fe(II) cations diffuse more favorably through the porous oxide film of ZVI toward to the contaminant species [8], it can be suggested that the iron nanoparticles probably operate as generators of reducing species (Fe(II), H/H_2) and removing agents (Fe hydroxides and oxides) than as direct reducing agents. Despite Fe(III) and Cr(III) that are produced in these reactions, co-precipitation of Cr(III)/Fe(III) in the form of $Cr_xFe_{1-x}(OH)_3$ or $Cr_xFe_{1-x}(OOH)$, $x < 1$ is also possible. The pH is a critical criterion in determining the thickness of the double layer at the interface between the oxide surface and solution [7]. Following these results, one can conclude that for the lower pH values, an increased reactivity is observed while the electron transfer is promoted and the passivation of the iron particles is hindered.

It should be noted that in all kinetic experiments, the hexavalent chromium reduction proceeded rapidly in the first 2 h while in the next hours, it was decelerated progressively. The lower pH values prevail in efficiency as it could be observed when the initial pH value of the solutions increases, the removal percentages of Cr(VI) decrease. Specifically, the efficiency of the nZVI@MCM-41 sample for the chromium removal after 9 h reaction time at pH = 3 was determined to be 100% for 180 mg/L while 64% was found for 100 mg/L of material dose (its kinetic is not shown in the figure). In addition, concerning the parent MCM-41 material, only at pH = 3, a small removal of Cr(VI) occurred, *i.e.*, ~6%.

Fig. 9c shows the effectiveness of the nZVI@MCM-41 sample in comparison to unsupported nZVI as a function of reaction time at pH = 3 and $[Cr(VI)]_0$ = 6 mg/L. In order to be comparable, the dose of the unsupported nZVI was chosen to be equal with the Fe^0 loading of the hybrid material (~9.3ɣwt%), as it was calculated according to the TGA results. It should be noted that, bared nZVI exhibit a significant slower and lower reaction rate (0.10 h^{-1}) with efficiency determined to be only 26% after 3 h of treatment while for the same time, the nZVI@MCM-41 material has removed 95% of Cr(VI) due to its higher reaction rate (1.02 h^{-1}).

Along these lines, the variation of pH during the reactions of Cr(VI) with nZVI and nZVI@MCM-41 at $pH_{initial}$ = 3 and 5 was determined and the results are presented in Fig. 10 (MCM-41 effect

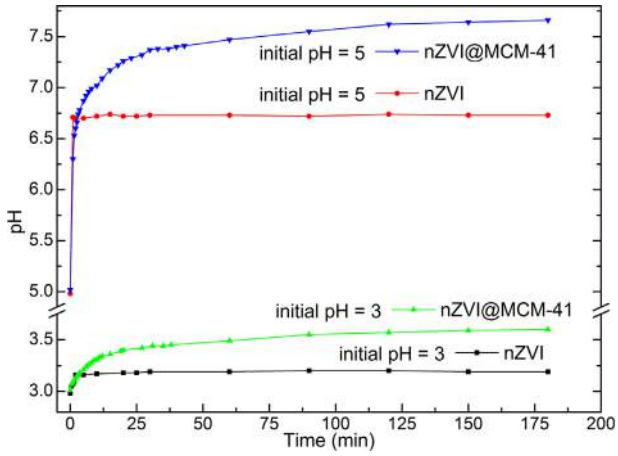

Fig. 10. Variation of pH during the reaction process of Cr(VI) by nZVI@MCM-41 and nZVI at initial pH values 3 and 5.

on pH in Supporting Information Fig. S4). As shown in this figure, the solution pH of nZVI@MCM-41 system originally increased to higher pH values (3.6 and 7.7 from $pH_{initial}$ 3 and 5, respectively) and reached a plateau with increasing the reaction time. These pH changes are similar to that of the nZVI "standalone" system. However, the use of MCM-41 as support material resulted to even higher pH values than those observed in the single nZVI treatment (3.2 and 6.7). These results are in agreement with those of a recently published work on degradation of trinitroglycerin using ZVI nanoparticles supported on SBA-15 [47]. These features are also commonly observed in the leading edge of zero-valent iron permeable reactive barriers (PRBs) and are due to abrupt depletion of protons during the ZVI oxidation. [73]. Normally, this described pH increase leads to the development of a passivation layer on the ZVI surface that can prevent the transport of Cr(VI) species to the underlying iron surface and, thus, their subsequent reduction. In previous studies concerning the mechanism of Cr(VI) reduction using ZVI supported on pillared bentonite or silica [55,73] an opposite pH trend has been observed during the same reaction and it has been assigned to buffering effect of aluminol or silanol groups on the support surfaces. According to that mechanism, as the pH increased with protons being consumed, the aluminol or silanol groups of support material, dissociated to compensate the depletion of protons. Thus, the generated protons maintained the pH close to the initial value, which in turn reduced the surface passivation of iron. In addition, negatively charged surface sites rendered by release of protons from aluminol or silanol groups may have served as collectors for iron cations, increasing the probability of co-precipitation of reaction products. In fact, as it has been reported, the bentonite and silica surface can strongly bind Fe(III) and Cr(III) *via* surface complexation [73–75].

On the other hand, considering the fact that mesoporous silica support of nZVI@MCM-41 has a pH_{pzc} equal to 3.2 [50] and as the solution initial pH (3 or 5) increases rapidly during the reaction (Fig. 10) to higher values, the MCM-41 surface will bear a progressively increasing negative charge, so the adsorption of Cr(VI) on it will be limited (Supporting Information Fig. S5). In contrast, at pH > 3.2 the MCM-41 negatively charged surface can act as scavenger but can enhance the reaction rate through its interaction with reaction precipitates (Fe^{3+}, Cr^{3+}).

In other words, MCM-41 could react as a scavenger for the precipitates and in that way, minimizing the agglomeration of the reduced products on the surface of nZVI, providing more free area for reaction, facilitated their well dispersion and non-agglomeration as well. This leads to a higher surface area and higher reactivity of zero-valent iron nanoparticles which are stabilized on the MCM-41 surface, exhibiting, thus, an improved efficiency for hexavalent chromium removal from aqueous solutions. In addition, the experimental results showed also a progressive increase of pH with the time that suggests a slower rate for nZVI passivation in nZVI@MCM-41 material in comparison to that for unsupported nZVI. Besides, the aqueous Cr(III) concentrations in the solutions after the reaction with nZVI@MCM-41 were calculated and found to be zero and 2 mg/L at pH values 5 and 3 respectively [54]. Considering, that the used initial amount of Cr(VI) was 6 mg/L and the removal efficiency of nZVI@MCM-41 was determined to be 100% (pH = 3) and 53% (pH = 5) it is obvious that 4 mg/L and 3.2 mg/L of insoluble species of Cr(III) precipitated on the surface of MCM-41 respectively. It can be reasonably assumed that the higher pH values observed during the reaction (Fig. 10) provided favorable conditions for the precipitation of Cr(III)/Fe(III) oxides/hydroxides on the high surface area of MCM-41 matrix.

4. Conclusions

Nanoscale zero-valent iron supported on surfaces of mesoporous MCM-41 silica have been prepared, characterized, and tested for Cr(VI) treatment. The synthesis method was based on borohydride reduction and use of a ferric chloride impregnating silica mesoporous matrix of the well known MCM-41 material. This preparation method leads to well dispersed and stabilized nanoscale zero-valent iron particles (nZVI) on a porous matrix which retains its ordered structural characteristics and exhibits a considerably high surface area (~600 m^2/g). The as-synthesized nanoparticles seems to possess a typical core–shell architecture of nZVI in which the core is consisted mainly of Fe^0 and the shell is largely of iron oxides/hydroxides origin formed from the oxidation of zero-valent iron. Transmission electron microscopy images showed the presence of homogeneously dispersed nZVI particles, elliptical in shape and with almost uniform sizes (60–80 nm), thought Mössbauer spectroscopy data also suggest the existence of smaller nanoparticles, which show superparamagnetic behavior due to their reduced sizes. In addition, the Mössbauer spectra of the samples treated with aquatic Cr(VI) solutions revealed that the size of nZVI is a significant factor for the yield of the reduction of chromium in the solution, as the smaller ZVI particles are simultaneously the most active to this procedure as well. Magnetization measurements showed that nZVI@MCM-41 sample exhibits ferromagnetic behavior with maximum magnetizations (at 7 T) of ~36.8 and 43.7 Am^2/kg at 300 and 5 K, respectively. The kinetic data are well fitted with a pseudo-first-order reaction model in order to adequately describe the kinetic uptake of Cr(VI) on nZVI@MCM-41. The results revealed that the synthesized material exhibits enhanced efficiency on Cr(VI) removal in comparison with nZVI particles, indicating a synergetic effect between reduction by nZVI and MCM-41 inducing precipitate formation of the reduced species. The hosting within the mesoporous silica matrix prevented agglomeration of the nanoscale iron and thus, increased its surface area allowing accessibility of the Cr(VI) species to the nZVI particles.

Acknowledgements

The authors acknowledge the support by the Operational Program Research and Development for Innovations – European Regional Development Fund (CZ.1.05/2.1.00/03.0058) and Operational Program Education for Competitiveness – European Social Fund (CZ.1.07/2.3.00/20.0017, CZ.1.07/2.3.00/20.0170, CZ.1.07/2.3.00/20.0155, and CZ.1.07/2.3.00/20.0056) of the Ministry of Education, Youth and Sports of the Czech Republic. We also thank Dr. Safarova for TEM observations.

Appendix A. Supplementary data

Supplementary data associated with this article can be found, in the online version, at http://dx.doi.org/10.1016/j.jhazmat.2013.07.046.

References

[1] X.Q. Li, D.W. Elliott, W.X. Zhang, Zero-valent iron nanoparticles for abatement of environmental pollutants, Critical Reviews in Solid State and Materials Sciences 31 (2006) 111–122.
[2] C. Noubactep, A critical review on the process of contaminant removal in Fe^0–H_2O systems, Environmental Technology 29 (2008) 909–920.
[3] Y.P. Sun, X.Q. Li, J. Cao, W.X. Zhang, H.P. Wang, Characterization of zero-valent iron nanoparticles, Advances in Colloid and Interface Science 120 (2006) 47–56.
[4] W.X. Zhang, Nanoscale iron particles for environmental remediation: an overview, Journal of Nanoparticle Research 5 (2003) 323–332.
[5] Ç. Üzüm, T. Shahwan, A.E. Eroğlu, I. Lieberwirth, T.B. Scott, K.R. Hallam, Application of zero-valent iron nanoparticles for the removal of aqueous Co^{2+} ions under various experimental conditions, Chemical Engineering Journal 144 (2008) 213–220.
[6] S.M. Ponder, J.G. Darab, J. Bucher, D. Caulder, I. Craig, L. Davis, N. Edelstein, W. Lukens, H. Nitsche, L. Rao, D.K. Shuh, T.E. Mallouk, Surface chemistry and electrochemistry of supported zerovalent iron nanoparticles in the remediation of aqueous metal contaminants, Chemistry of Materials 13 (2001) 479–486.
[7] C. Noubactep, S. Caré, R.A. Crane, Nanoscale metallic iron for environmental remediation: prospects and limitations, Water, Air, and Soil Pollution 223 (2012) 1363–1382.
[8] C. Noubactep, An analysis of the evolution of reactive species in Fe^0/H_2O systems, Journal of Hazardous Materials 168 (2009) 1626–1631.
[9] M. Stratmann, J. Müller, The mechanism of the oxygen reduction on rust-covered metal substrates, Corrosion Science 36 (1994) 327–359.
[10] R.A. Crane, T.B. Scott, Nanoscale zero-valent iron: future prospects for an emerging water treatment technology, Journal of Hazardous Materials 211–212 (211) (2012) 112–120.
[11] A. Fiúza, A. Silva, G. Carvalho, A.V. de la Fuente, C. Delerue-Matos, Heterogeneous kinetics of the reduction of chromium (VI) by elemental iron, Journal of Hazardous Materials 175 (2010) 1042–1047.
[12] M. Muthukrishnan, B.K. Guha, Effect of pH on rejection of hexavalent chromium by nanofiltration, Desalination 219 (2008) 171–178.
[13] C.H. Weng, Y.T. Lin, T.Y. Lin, C.M. Kao, Enhancement of electrokinetic remediation of hyper-Cr(VI) contaminated clay by zero-valent iron, Journal of Hazardous Materials 149 (2007) 292–302.
[14] M. Costa, Potential hazards of hexavalent chromate in our drinking water, Toxicology and Applied Pharmacology 188 (2003) 1–5.
[15] J. Cerulli, D.W. Grabe, I. Gauthier, M. Malone, M.D. McGoldrick, Chromium picolinate toxicity, Annals of Pharmacotherapy 32 (1998) 428–431.
[16] M.D. Stearns, M.S. Silveira, K.K. Wolf, Chromium(III) tris(picolinate) is mutagenic at the hypoxanthine (guanine) phosphoribosyltransferase locus in Chinese hamster ovary cells, Mutation Research 513 (2002) 135–142.
[17] S.A. Kareus, C. Kelley, H.S. Walton, P.R. Sinclair, Release of Cr(III) from Cr(III) picolinate upon metabolic activation, Journal of Hazardous Materials B84 (2001) 163–174.
[18] M. Gheju, A. Iovi, I. Balcu, Hexavalent chromium reduction with scrap iron in continuous-flow system. Part 1: effect of feed solution pH, Journal of Hazardous Materials 153 (2008) 655–662.
[19] M. Gheju, I. Balcu, Hexavalent chromium reduction with scrap iron in continuous-flow system. Part 2: effect of scrap iron shape and size, Journal of Hazardous Materials 182 (2010) 484–493.
[20] M. Gheju, I. Balcu, Removal of chromium from Cr(VI) polluted wastewaters by reduction with scrap iron and subsequent precipitation of resulted cations, Journal of Hazardous Materials 196 (2011) 131–138.
[21] D. O'Carroll, B. Sleep, M. Krol, H. Boparai, C. Kocur, Nanoscale zero valent iron and bimetallic particles for contaminated site remediation, Advances in Water Resources 51 (2013) 104–122.
[22] M.M. Scherer, S. Richter, R.L. Valentine, P.J.J. Alvarez, Chemistry, Microbiology of permeable reactive barriers for in situ groundwater clean up, Critical Reviews in Microbiology 26 (2000) 221–264.
[23] Y.P. Sun, X.Q. Li, W.X. Zhang, H.P. Wang, A method for the preparation of stable dispersion of zero-valent iron nanoparticles, Colloids and Surfaces A 308 (2007) 60–66.
[24] A. Tiraferri, K.L. Chen, R. Sethi, M. Elimelech, Reduced aggregation and sedimentation of zero-valent iron nanoparticles in the presence of guar gum, Journal of Colloid and Interface Science 324 (2008) 71–79.
[25] K. Siskova, J. Tucek, L. MacHala, E. Otyepkova, Air-stable nZVI formation mediated by glutamic acid: solid-state storable material exhibiting 2D chain morphology and high reactivity in aqueous environment, Journal of Nanoparticle Research 14 (2012) 1–13.
[26] R. Zboril, M. Andrle, F. Oplustil, L. Machala, J. Tucek, J. Filip, Z. Marusak, V.K. Sharma, Treatment of chemical warfare agents by zero-valent iron nanoparticles and ferrate(VI)/(III) composite, Journal of Hazardous Materials 211–212 (2012) 126–130.
[27] S.-C. Tsai, Heavy Metal Removal From Water by Zero-valent Iron, Department and Graduate Institute of Environmental Engineering and Management, 2012 (Master's Thesis).
[28] H. Zhang, Z.H. Jin, L. Han, C.H. Qin, Synthesis of nanoscale zero-valent iron supported on exfoliated graphite for removal of nitrate, Transactions of Nonferrous Metals Society of China 16 (2006) s345–s349.
[29] L. Li, M. Fan, R. Brown, J. Van Leeuwen, J. Wang, W. Wang, Y. Song, P. Zhang, Synthesis, properties and environmental applications of nanoscale iron-based materials: a review, Critical Reviews in Environmental Science and Technology 36 (2006) 405–431.
[30] Ç. Üzüm, T. Shahwan, A.E. Eroğlu, K.R. Hallam, T.B. Scott, I. Lieberwirth, Synthesis and characterization of kaolinite-supported zero-valent iron nanoparticles and their application for the removal of aqueous Cu^{2+} and Co^{2+} ions, Applied Clay Science 43 (2009) 172–181.
[31] P. Wu, S. Li, L. Ju, N. Zhu, J. Wu, P. Li, Z. Dang, Mechanism of the reduction of hexavalent chromium by organo-montmorillonite supported iron nanoparticles, Journal of Hazardous Materials 219–220 (2012) 283–288.
[32] X. Qiu, Z. Fang, B. Liang, F. Gu, Z. Xu, Degradation of decabromodiphenyl ether by nano zero-valent iron immobilized in mesoporous silica microspheres, Journal of Hazardous Materials 193 (2011) 70–81.
[33] Y. Li, Z. Jin, T. Li, S. Li, Removal of hexavalent chromium in soil and groundwater by supported nano zero-valent iron on silica fume, Water Science and Technology 63 (2011) 2781–2787.
[34] J. Zhan, T. Zheng, G. Piringer, C. Day, G.L. McPherson, Y. Lu, K. Papadopoulos, V.T. John, Transport characteristics of nanoscale functional zerovalent iron/silica composites for in situ remediation of trichloroethylene, Environmental Science and Technology 42 (2008) 8871–8876.
[35] Y. Zhang, Y. Li, J. Li, G. Sheng, Y. Zhang, X. Zheng, Enhanced Cr(VI) removal by using the mixture of pillared bentonite and zero-valent iron, Chemical Engineering Journal 185–186 (2012) 243–249.
[36] Y. Zhang, Y. Li, J. Li, L. Hu, X. Zheng, Enhanced removal of nitrate by a novel composite: nanoscale zero valent iron supported on pillared clay, Chemical Engineering Journal 171 (2011) 526–531.
[37] H. Kim, H.J. Hong, Y.J. Lee, H.J. Shin, J.W. Yang, Degradation of trichloroethylene by zero-valent iron immobilized in cationic exchange membrane, Desalination 223 (2008) 212–220.
[38] D.E. Meyer, K. Wood, L.G. Bachas, D. Bhattacharyya, Degradation of chlorinated organics by membrane-immobilized nanosized metals, Environmental Progress 23 (2004) 232–242.
[39] H.-Y. Shu, M.-C. Chang, C.-C. Chen, P.-E. Chen, Using resin supported nano zero-valent iron particles for decoloration of Acid Blue 113 azo dye solution, Journal of Hazardous Materials 184 (2010) 499–505.
[40] H. Kim, H.-J. Hong, J. Jung, S.-H. Kim, J.-W. Yang, Degradation of trichloroethylene (TCE) by nanoscale zero-valent iron (nZVI) immobilized in alginate bead, Journal of Hazardous Materials 176 (2010) 1038–1043.
[41] T. Liu, L. Zhao, D. Sun, X. Tan, Entrapment of nanoscale zero-valent iron in chitosan beads for hexavalent chromium removal from wastewater, Journal of Hazardous Materials 184 (2010) 724–730.
[42] V. Madhavi, A.V.B. Reddy, K.G. Reddy, G. Madhavi, A simple method for the determination of efficiency of stabilized Fe^0 nanoparticles for detoxification of chromium (VI) in water, Journal of Chemical and Pharmaceutical Research 4 (2012) 1539–1545.
[43] H. Zhu, Y. Jia, X. Wu, H. Wang, Removal of arsenic from water by supported nano zero-valent iron on activated carbon, Journal of Hazardous Materials 172 (2009) 1591–1596.
[44] F.J. Zhang, H. Xuan, F.Z. Xie, T. Jiang, T. Chen, W.C. Oh, Enhancing decolorization for methyl orange in aqueous solution by graphene supported nanoscale zero valent iron, Asian Journal of Chemistry 24 (2012) 3994–3996.
[45] X. Ling, J. Li, W. Zhu, Y. Zhu, X. Sun, J. Shen, W. Han, L. Wang, Synthesis of nanoscale zero-valent iron/ordered mesoporous carbon for adsorption and synergistic reduction of nitrobenzene, Chemosphere 87 (2012) 655–660.
[46] J. Li, H. Li, Y. Zhu, Y. Hao, X. Sun, L. Wang, Dual roles of amphiphilic triblock copolymer P123 in synthesis of α-Fe nanoparticle/ordered mesoporous silica composites, Applied Surface Science 258 (2011) 657–661.
[47] R. Saad, S. Thiboutot, G. Ampleman, W. Dashan, J. Hawari, Degradation of trinitroglycerin (TNG) using zero-valent iron nanoparticles/nanosilica SBA-15 composite (ZVINs/SBA-15), Chemosphere 81 (2010) 853–858.
[48] P. Zhang, X. Tao, Z. Li, R.S. Bowman, Enhanced perchloroethylene reduction in column systems using surfactant-modified zeolite/zero-valent iron pellets, Environmental Science and Technology 36 (2002) 3597–3603.
[49] T. Zheng, J. Zhan, J. He, C. Day, Y. Lu, G.L. McPherson, G. Piringer, V.T. John, Reactivity characteristics of nanoscale zerovalent iron-silica composites for trichloroethylene remediation, Environmental Science and Technology 42 (2008) 4494–4499.
[50] K. Dimos, P. Stathi, M.A. Karakassides, Y. Deligiannakis, Synthesis and characterization of hybrid MCM-41 materials for heavy metal adsorption, Microporous and Mesoporous Materials 126 (2009) 65–71.
[51] P. Stathi, K. Dimos, M.A. Karakassides, Y. Deligiannakis, Mechanism of heavy metal uptake by a hybrid MCM-41 material: surface complexation and EPR spectroscopic study, Journal of Colloid and Interface Science 343 (2010) 374–380.
[52] A.B. Bourlinos, A. Simopoulos, N. Boukos, D. Petridis, Magnetic modification of the external surfaces in the MCM-41 porous silica: synthesis, characterization, and functionalization, Journal of Physical Chemistry B 105 (2001) 7432–7437.

[53] D.J. Fyfe, Rapid, automated and cost-effective analyses of hexavalent chromium for WEEE/RoHS using the Varian Cary 50 UV–Vis Microplate Reader System, Varian Inc. Application Note 00533.
[54] APHA, AWWA, WEF, Standard Methods for the Examination of Water and Wastewater, 21st ed., United Book Press, Inc., Baltimore, MD, 2005.
[55] Y. Li, J. Li, Y. Zhang, Mechanism insights into enhanced Cr(VI) removal using nanoscale zerovalent iron supported on the pillared bentonite by macroscopic and spectroscopic studies, Journal of Hazardous Materials 227–228 (2012) 211–218.
[56] K. Dimos, L. Jankovič, I.B. Koutselas, M.A. Karakassides, R. Zbořil, P. Komadel, Low-temperature synthesis and characterization of gallium nitride quantum dots in ordered mesoporous silica, Journal of Physical Chemistry C 116 (2012) 1185–1194.
[57] C.T. Kirk, Quantitative analysis of the effect of disorder-induced mode coupling on infrared absorption in silica, Physical Review B 38 (1988) 1255–1273.
[58] P.G. Pai, S.S. Chao, Y. Takagi, G. Lucovsky, Infrared spectroscopic study of SiO_x films produced by plasma enhanced chemical vapor deposition, Journal of Vacuum Science and Technology A 4 (1986) 689–694.
[59] M.R. Almeida, C.G. Pantano, Structural investigation of silica gel films by infrared spectroscopy, Journal of Applied Physics 68 (1990) 4225–4232.
[60] E.I. Kamitsos, A.P. Patsis, G. Kordas, Infrared-reflectance spectra of heat-treated sol–gel-derived silica, Physical Review B 48 (1993) 12499–12505.
[61] K. Dimos, M.K. Antoniou, A. Meichanetzoglou, S. Lymperopoulou, M.-D. Ouzouni, I.B. Koutselas, D. Fokas, M.A. Karakassides, R.G. Agostino, D. Gournis, Naphthalene-based periodic nanoporous organosilicas: I. Synthesis and structural characterization, Microporous and Mesoporous Materials 158 (2012) 324–331.
[62] A. Jitianu, M. Crisan, A. Meghea, I. Rau, M. Zaharescu, Influence of the silica based matrix on the formation of iron oxide nanoparticles in the Fe_2O_3–SiO_2 system, obtained by sol–gel method, Journal of Materials Chemistry 12 (2002) 1401–1407.
[63] D. Wen, P. Song, K. Zhang, J. Qian, Thermal oxidation of iron nanoparticles and its implication for chemical-looping combustion, Journal of Chemical Technology and Biotechnology 86 (2011) 375–380.
[64] Y. Li, Y. Zhang, J. Li, X. Zheng, Enhanced removal of pentachlorophenol by a novel composite: nanoscale zero valent iron immobilized on organobentonite, Environmental Pollution 159 (2011) 3744–3749.
[65] S. Mørup, Mössbauer effect in small particles, Hyperfine Interactions 60 (1990) 959–974.
[66] N.N. Greenwood, T.C. Gibb, Mössbauer Spectroscopy, Chapman and Hall Ltd., London, 1971.
[67] A.P. Douvalis, R. Zboril, A.B. Bourlinos, J. Tucek, S. Spyridi, T. Bakas, A facile synthetic route toward air-stable magnetic nanoalloys with Fe-Ni/Fe-Co core and iron oxide shell, Journal of Nanoparticle Research 14 (2012), 1130(1–16).
[68] B.D. Cullity, C.D. Graham, Introduction to Magnetic Materials, Wiley, NJ, 2009.
[69] L.-N. Shi, X. Zhang, Z.-L. Chen, Removal of Chromium (VI) from wastewater using bentonite-supported nanoscale zero-valent iron, Water Research 45 (2011) 886–892.
[70] M. Baikousi, A.B. Bourlinos, A. Douvalis, T. Bakas, D.F. Anagnostopoulos, J. Tuček, K. Šafářová, R. Zboril, M.A. Karakassides, Synthesis and characterization of γ-Fe_2O_3/carbon hybrids and their application in removal of hexavalent chromium ions from aqueous solutions, Langmuir 28 (2012) 3918–3930.
[71] X.-Q. Li, J. Cao, W.-X. Zhang, Stoichiometry of Cr(VI) immobilization using nanoscale zerovalent iron (nZVI): a study with high-resolution X-ray photoelectron spectroscopy (HR-XPS), Industrial and Engineering Chemistry Research 47 (2008) 2131–2139.
[72] M. Odziemkowski, Spectroscopic studies and reactions of corrosion products at surfaces and electrodes, Spectroscopic Properties of Inorganic and Organometallic Compounds 40 (2009) 385–449.
[73] Y.J. Oh, H. Song, W.S. Shin, S.J. Choi, Y.-H. Kim, Effect of amorphous silica and silica sand on removal of chromium(VI) by zero-valent iron, Chemosphere 66 (2007) 858–865.
[74] S.E. Fendorf, G.M. Lamble, M.G. Stapleton, M.J. Kelley, D.L. Sparks, Mechanisms of chromium(III) sorption on silica. 1. Chromium(III) surface structure derived by extended X-ray absorption fine structure spectroscopy, Environmental Science and Technology 28 (1994) 284–289.
[75] K. Flogeac, E. Guillon, M. Aplincourt, Adsorption of several metal ions onto a model soil sample: equilibrium and EPR studies, Journal of Colloid and Interface Science 286 (2005) 596–601.